Electrochimica Acta 511 (2025) 145363

Contents lists available at ScienceDirect

Electrochimica Acta

journal homepage: www.journals.elsevier.com/electrochimica-acta

An experimentally validated numerical model of pH changes in surrogate tissue induced by electroporation pulses

Rok Šmerc, Damijan Miklavčič, Samo Mahnič-Kalamiza *

University of Ljubljana, Faculty of Electrical Engineering, Tržaška cesta 25, SI-1000 Ljubljana, Slovenia

ARTICLE INFO

Keywords:
Electrochemistry
Mathematical model
Electroporation
pH front
Agarose gel phantoms
Hydrolysis

ABSTRACT

Electroporation often leads to electrochemical reactions at the electrode-electrolytic solution interface, particularly when using monophasic pulses of considerable duration (typically on the order of several microseconds or longer) that cause not only capacitive charging of the double-layer, but also faradaic charge transfer between the electrodes and the solution. Applications, where the electrochemical changes are to be either avoided or actively exploited to benefit the treatment, range from gene electrotransfer to electrolytic ablation of tissue. Through numerical modelling and experimental validation, our study explores the extent of pH changes induced by faradaic currents in a surrogate tissue. A mechanistic multiphysics model of pH changes was developed based on first principles, incorporating hydrolysis reactions at the anode and cathode, and the Nernst-Planck model of ion transport. The model was validated using agarose gel tissue phantoms designed to simulate unbuffered and buffered (mimicking in vivo tissue buffering capacity) conditions. An imaging system with pH-sensitive dyes was developed and used to visualise and quantify pH front formation and migration. The model predictions qualitatively aligned well with experimental data, differentiating pH front behaviour between unbuffered and buffered media. However, the quantitative accuracy in predicting the temporal and spatial evolution of the pH fronts can be further improved. Experimental observations emphasise the need for more advanced models. Nevertheless, the developed model provides a sound theoretical foundation for predicting pH changes due to high-voltage electric pulse delivery, such as encountered in electroporation-based treatments and therapies.

1. Introduction

Electroporation is a biophysical phenomenon in which short, high-voltage electric pulses are used to transiently permeabilise the cell plasma membrane, facilitating the transport of ions and molecules across the membrane, and is often used to introduce various drugs and nucleic acids into the cells [1–3]. This phenomenon has shown great promise in various fields of biomedicine, biotechnology, and food processing [4–10]. Electroporation can be either reversible or irreversible, depending on the amplitude and duration of the pulses. Reversible electroporation temporarily disrupts the cell membrane and is utilised, for example, in gene electrotransfer and drug delivery [11,12]. Irreversible electroporation, on the other hand, leads to cell death and is used in tissue ablation, particularly in tumour treatment, and more recently also in the treatment of cardiac arrhythmias, particularly atrial fibrillation [10,13–17].

Electroporation in tissue is achieved by applying high-voltage (often accompanied by high-current) electric pulses via electrodes. These high-voltage (high-current) pulses also cause heating in the tissue and electrochemical reactions at the electrode-electrolyte interface [18,19]. While electroporation and tissue heating have been extensively studied, the changes in pH and their effects are still relatively unexplored [20–23]. In tissue, pH changes are caused by the electrolysis of water, i.e., hydrolysis. Hydrolysis leads to significant pH changes at the electrode-electrolyte or electrode-electrolytic solution interface, resulting in extreme local pH changes [24–27]. The pH changes in tissue may be important in e.g. gene electrotransfer, where control of pH conditions is crucial for maintaining the stability of plasmid DNA. Extreme pH changes can negatively affect transfection efficiency by, in the most extreme case, denaturing the plasmid DNA, but also affecting cell viability [28,29]. For successful gene expression, it is thus critical to minimise pH changes, and thus plasmid DNA and tissue damage [12,29,30].

Conversely, pH changes were recognised as the main mechanism of action in the electrochemical treatment of tumours. This approach uses low-level DC to establish acidic and alkaline environments and cause

* Corresponding author at: University of Ljubljana, Faculty of Electrical Engineering, Laboratory of Biocybernetics, Tržaška cesta 25, SI-1000 Ljubljana Slovenia.
E-mail address: samo.mahnic-kalamiza@fe.uni-lj.si (S. Mahnič-Kalamiza).

https://doi.org/10.1016/j.electacta.2024.145363
Received 22 August 2024; Received in revised form 28 October 2024; Accepted 15 November 2024
Available online 16 November 2024
0013-4686/© 2024 The Author(s). Published by Elsevier Ltd. This is an open access article under the CC BY-NC license (http://creativecommons.org/licenses/by-nc/4.0/).

cell death [31–36]. Recently, it has been suggested that the combined use of electroporation and electrolysis, termed E2, enhances cell death and consequently tissue ablation by allowing the electrolytic products to enter into the cell through a permeabilised cell membrane, thereby reducing the required charge and treatment duration [37–40]. Furthermore, it was shown that ablation volumes comparable to conventional irreversible electroporation (using high-voltage pulses) can also be achieved with a larger number of low-voltage pulses, suggesting that electrolysis and pH changes contribute significantly to cell death [41]. On the other hand, the use of sub-microsecond electric pulses in electrochemotherapy has shown that these pulses reduce heating and electrochemical reactions, although requiring higher concentrations of chemotherapeutic agents for similar cytotoxic effects [42]. Additionally, sub-microsecond electric pulses have been shown to be effective in gene electrotransfer [29,43], a therapy that would also benefit from the reduced heating and electrochemical reactions associated with sub-microsecond pulses.

Computational models show that pulse amplitude and polarity significantly influence the dissolution of metal electrodes, highlighting the importance of optimising these parameters. Recent studies using a multiphysics approach have further explored the electrochemical effects and electrode material alterations in electroporation, giving important insights into the underlying mechanisms [18,44]. Furthermore, magnetic resonance imaging and electrical impedance tomography have been used to monitor pH changes during electrolysis in real-time [45,46]. Understanding the significance of pH changes is also crucial in the field of pulsed electric field (PEF) treatments of foods as they affect the inactivation of microbes, enzymes, and cause electrode corrosion. By optimising the pulse waveforms, undesirable electrochemical reactions can be minimised [47,48]. Finally, multiphysics modelling has provided insight into the effects of pulse frequency and medium composition on metal release from the electrodes, enabling optimisation of PEF treatment conditions to reduce electrode degradation [49].

Pioneering work in modelling electrochemical treatments was done by Eva Nilsson et al. for both the unbuffered and buffered electrolytes. Their models are based on the Nernst-Planck system of equations [24,25,32,33]. Subsequent studies have made important contributions by investigating pH-front interaction in tissue, the optimal dose-response relationship, innovative electrode configurations, protein denaturation dynamics, and comprehensive 2D modelling [50–56]. However, these models specifically address the electrical conditions typical of the electrochemical treatment of tumours, in which direct currents of low amplitudes are applied over a longer period, often up to several hours [34]. In contrast, electroporation uses short, high-amplitude pulses, which require careful setup of the numerical methods of resolving the model, as the pulses of high amplitude in both voltage (and often current) make the simulation inherently unstable. Consequently, recent studies have focused on the computational modelling of pH changes during electroporation. Electroporation has been shown to create significant and immediate formation of pH fronts that can lead to tissue damage if not controlled [26,57,58]. It has also been suggested that pH fronts are the primary cause of muscle damage in gene electrotransfer protocols [27,59]. Additionally, a dose-response model linking pulse dosage to tissue damage was developed [60]. Overall, these studies highlight the crucial role of modelling in optimising and understanding electrochemical processes involved in the treatment.

The aim of our study was thus to build a comprehensive mechanistic computational model of pH changes in tissue during and after the application of electric pulses with parameters typical of electroporation as used in gene electrotransfer (milliseconds-duration monophasic pulses). The developed model was validated by experiments using agarose gels to which various pH indicators were added to monitor pH changes. In addition, a video recording system was developed and calibrated to allow for a direct comparison between the experimental results and the model calculations. The aim of this approach was to establish reliable reproducible experimental protocols and to validate the computational model and ensure its accuracy and applicability in predicting pH changes during electroporation.

2. Materials and methods

2.1. Governing equations and transport mechanisms

The Nernst-Planck equation system, which describes the transport of ionic species and the distribution of the electric potential in the electrolyte, was used as a framework for the model. Two configurations were analysed: an unbuffered model and a buffered model, based on previous work [24,25,27,32,33]. For the unbuffered model, the system consists of equations for the concentration of ions in a four-component electrolyte, where the components are hydrogen (H^+), hydroxide (OH^-), chloride (Cl^-), and sodium ions (Na^+), along with an equation for the spatial distribution of the electric potential (ϕ). The system, therefore, consists of five coupled partial differential equations. These equations consider two mechanisms of ion transport, namely diffusion, which is driven by concentration gradients, and migration, which is driven by the gradient of the electric potential. Convection is considered negligible and is therefore not considered in the model. This assumption is likely valid under in vivo conditions due to the phenomenon of the vascular lock, wherein electroporation pulses cause a temporary and localised cessation of perfusion, effectively immobilising the pH-altering products within the treated area [61]. The buffered model contains a bicarbonate buffer which expands the electrolyte to a seven-component system by adding bicarbonate (HCO_3^-) and carbonate ions (CO_3^{2-}), and carbon dioxide (CO_2) to the components of the unbuffered model. This leads to a system of eight coupled partial differential equations, introducing additional complexity and numerical stability challenges.

The mass balance of the ions of species i is defined as

$$\frac{\partial c_i}{\partial t} = -\nabla\cdot\mathbf{N}_i + R_i, \tag{1}$$

where c_i is the ion concentration of species i, t is the time, R_i is the production of species i by chemical reactions in the electrolyte, and $\mathbf{N}_i$ is the molar flux of ions of species i, defined as

$$\mathbf{N}_i = -D_i\nabla c_i - \frac{z_i}{|z_i|}u_i c_i \nabla\phi, \tag{2}$$

where D_i is the ion diffusion coefficient of the species i, z_i is the charge of the species i, u_i is the ion mobility of the species i, and ϕ is the electric potential in the electrolyte. The first term in Eq. (2) describes the mechanism of diffusion, and the second term describes electrophoresis, i.e., the migration of charged species due to the electric field. Ion mobility and the diffusion coefficient are linked by the Nernst-Einstein equation

$$D_i = \frac{RT}{|z_i|F}u_i, \tag{3}$$

where T is the temperature, R the universal gas constant, and F the Faraday constant. The last differential equation used is the equation for the conservation of electric charge

$$\nabla\left(\sum_{i=1}^{N}|z_i|u_i c_i\nabla\phi\right) + \sum_{i=1}^{N} z_i D_i \nabla^2 c_i = 0. \tag{4}$$

Note: the upper bound N of summation in Eq. (4) depends on whether the buffer is considered: $N = 4$ in the unbuffered model and $N = 7$ in the buffered model, respectively. Finally, the condition of electroneutrality must be considered

$$\sum_{i=1}^{N} z_i c_i = 0. \tag{5}$$

During pulse delivery, oxidation (i.e., electron loss) takes place at the anode and reduction (i.e., electron gain) at the cathode. When platinum is used as an electrode material in biological tissue, the anodic reactions consist mainly of the production of oxygen and chlorine gases, while hydrogen gas is released at the cathode. The main reactions at the anode are therefore oxygen and chlorine evolution

$$2H_2O \rightleftharpoons O_{2(g)} + 4H^+ + 4e^-, \tag{6}$$

$$2Cl^- \rightleftharpoons Cl_{2(g)} + 2e^-, \tag{7}$$

while the main reaction at the cathode is hydrogen evolution

$$2H_2O + 2e^- \rightleftharpoons H_{2(g)} + 2OH^-. \tag{8}$$

In the case of the unbuffered model, only one chemical reaction is considered, the water autoprotolysis reaction

$$H^+ + OH^- \underset{k_{w,b}}{\overset{k_{w,f}}{\rightleftharpoons}} H_2O. \tag{9}$$

In the buffered model, however, three additional chemical reactions are considered

$$H^+ + HCO_3^- \underset{k_{b1,b}}{\overset{k_{b1,f}}{\rightleftharpoons}} CO_2 + H_2O, \tag{10}$$

$$OH^- + CO_2 \underset{k_{b2,b}}{\overset{k_{b2,f}}{\rightleftharpoons}} HCO_3^-, \tag{11}$$

$$OH^- + HCO_3^- \underset{k_{b3,b}}{\overset{k_{b3,f}}{\rightleftharpoons}} CO_3^{2-} + H_2O. \tag{12}$$

Appendix A provides the additional equations that define the production of ionic species, as well as the boundary and initial conditions for the numerical model.

2.2. Computational approach

The system of equations defined above was solved using the finite element method in the COMSOL Multiphysics (COMSOL Inc., Sweden) software environment, utilising the Tertiary Current Distribution, Nernst-Planck physics interface. A one-dimensional geometry was chosen as it represents a reasonable approximation of the experimental system as described below. In particular, the experimental setup was such that the electric field is mainly oriented parallel to the line connecting the anode with the cathode. This simplification to one dimension captures the essential physics of the problem without unnecessarily elevating the degree of computational complexity, since ion transport occurs predominantly along this axis. Consequently, variations in the two directions perpendicular to the main axis have a negligible effect on the overall results. This geometry was represented in the model as a line of 14.3 mm in length, which corresponds to the edge-to-edge distance between the electrodes in the experiments. The anodic boundary conditions were set at $x = 0$ mm, and the cathodic boundary conditions at $x = 14.3$ mm. The geometry was discretised into 14,924 mesh elements, employing cubic shape functions for both concentration and electric potential discretisation. The chosen pulse waveform consisted of 8 rectangular pulses with a duration of 10 ms each, delivered at a repetition rate of 1 s^{-1}. Two different amplitudes were used for the pulses: 200 V and 400 V, corresponding to 140 V/cm and 280 V/cm voltage-to-distance ratio, respectively. The simulations were performed using time-dependent studies in COMSOL Multiphysics, with the solver settings optimised to ensure convergence and accuracy. The values of all parameters required for the simulations are listed in Table 1. Post-processing of the simulation results was performed using Python.

2.3. Experimental setup

The experimental setup comprised a camera system, a pulse generator, an oscilloscope, and a PC. A Basler Ace ACA1920–155UC camera, which is capable of recording at 100 frames per second with a resolution

Table 1
Parameters and their corresponding values used in the models [24,25,62].

Parameter	Value	Unit	Description
$c^0_{H^+}$	$1.0 \cdot 10^{-4}$ (unbuffered) / $10^{-4.4}$ (buffered)	mol m^{-3}	Initial concentration of H^+
$c^0_{OH^-}$	$1.0 \cdot 10^{-4}$(unbuffered) / $10^{-3.2}$ (buffered)	mol m^{-3}	Initial concentration of OH^-
$c^0_{Na^+}$	160	mol m^{-3}	Initial concentration of Na^+
$c^0_{Cl^-}$	160 (unbuffered) / 132.9 (buffered)	mol m^{-3}	Initial concentration of Cl^-
$c^0_{HCO_3^-}$	27.0	mol m^{-3}	Initial concentration of HCO_3^-
$c^0_{CO_3^{2-}}$	$4.4 \cdot 10^{-2}$	mol m^{-3}	Initial concentration of CO_3^{2-}
$c^0_{CO_2}$	1.3	mol m^{-3}	Initial concentration of CO_2
D_{H^+}	$12.50 \cdot 10^{-9}$	m^2 s^{-1}	Diffusion coefficient of H^+
D_{OH^-}	$7.05 \cdot 10^{-9}$	m^2 s^{-1}	Diffusion coefficient of OH^-
D_{Na^+}	$1.78 \cdot 10^{-9}$	m^2 s^{-1}	Diffusion coefficient of Na^+
D_{Cl^-}	$2.72 \cdot 10^{-9}$	m^2 s^{-1}	Diffusion coefficient of Cl^-
$D_{HCO_3^-}$	$1.49 \cdot 10^{-9}$	m^2 s^{-1}	Diffusion coefficient of HCO_3^-
$D_{CO_3^{2-}}$	$2.46 \cdot 10^{-9}$	m^2 s^{-1}	Diffusion coefficient of CO_3^{2-}
D_{CO_2}	$2.71 \cdot 10^{-9}$	m^2 s^{-1}	Diffusion coefficient of CO_2
$k_{w,f}$	$1.5 \cdot 10^8$	m^3 mol^{-1} s^{-1}	Forward rate constant of water autoprotolysis reaction
$k_{w,b}$	$6.79 \cdot 10^{-5}$	s^{-1}	Backward rate constant of water autoprotolysis reaction
$k_{b1,f}$	310	m^3 mol^{-1} s^{-1}	Forward rate constant of 1st buffer reaction
$k_{b1,b}$	$4.62 \cdot 10^{-6}$	m^3 mol^{-1} s^{-1}	Backward rate constant of 1st buffer reaction
$k_{b2,f}$	20	m^3 mol^{-1} s^{-1}	Forward rate constant of 2nd buffer reaction
$k_{b2,b}$	$6.08 \cdot 10^{-4}$	s^{-1}	Backward rate constant of 2nd buffer reaction
$k_{b3,f}$	$1.5 \cdot 10^8$	m^3 mol^{-1} s^{-1}	Forward rate constant of 3rd buffer reaction
$k_{b3,b}$	$5.81 \cdot 10^7$	s^{-1}	Backward rate constant of 3rd buffer reaction
j^0_I	$1 \cdot 10^{-6}$	A m^{-2}	Exchange current density of oxygen evolution reaction
j^0_{II}	10	A m^{-2}	Exchange current density of chlorine evolution reaction
j^0_{III}	1	A m^{-2}	Exchange current density of hydrogen evolution reaction
E^{eq}_I	1.229	V	Equilibrium potential difference of oxygen evolution reaction
E^{eq}_{II}	1.36	V	Equilibrium potential difference of chlorine evolution reaction
E^{eq}_{III}	−0.828	V	Equilibrium potential difference of hydrogen evolution reaction

of 1920 × 1200 pixels, was employed to capture the rate of change in colour across the gel(s). The camera was equipped with a Basler C10–3514–8M-S f35 mm lens and was mounted on a Kaiser Copylizer exe.cutive LED – Kaiser 5215 stand, which features an illuminated base to ensure consistent lighting conditions throughout each experiment. The laboratory prototype pulse generator (HV-LV) [63] was used to deliver the pulses. The oscilloscope (HDO6104A-MS, LeCroy, USA) with voltage (HVD3206A, LeCroy, USA) and current (CP031A, LeCroy, USA) probes were used to monitor and verify the electric pulses generated by the pulse generator. The camera was connected to a PC, with which the video recordings of the experiments were recorded and saved. A photo of the experimental setup is shown in Fig. 1.

2.4. Camera system calibration experiments

The aim of the camera system calibration experiments was to develop a function capable of converting the colour information captured by the camera during the agarose gel experiments into numerical pH values for each pixel. A total of 27 different buffer solutions were prepared by mixing various weak acids with their conjugate bases, resulting in buffers with pH values between 1.0 and 13.0. Each buffer solution was verified using a calibrated pH metre to ensure accuracy. Three millilitres of each buffer solution were pipetted into a small Petri dish with a diameter of 34 mm. Then, 0.3 ml of a universal pH indicator solution was added to each Petri dish. The universal pH indicator was prepared with the following concentrations: 0.012 % methyl red, 0.06 % bromothymol blue, and 0.010 % phenolphthalein disodium salt. This indicator was chosen for its ability to display a wide range of colours and thus distinguish a broad spectrum of pH values. To facilitate the calibration experiments, the addition of agarose was omitted, as preliminary experiments showed that the agarose in the concentration used (i.e., 0.6 %) had no influence on the colour hue of the solutions. The solutions were then photographed with the camera system. Consistent lighting conditions were maintained throughout the experiments. The captured photographs were analysed to calculate the average RGB (red, green, blue) values of the pixels for each Petri dish. These RGB values were then converted into the HSV (hue, saturation, value) colour system, focusing on the hue component. The hue component, representing the angle on a 360-degree colour wheel corresponding to the perceived colour, was derived from the RGB values using the following formula:

$$h_{\mathrm{RGB}} = \mathrm{atan2}\left(\sqrt{3}\cdot(G-B), 2\cdot R - G - B\right). \tag{13}$$

Once the hue values corresponding to each pH value were determined, a calibration curve was established for the camera system by fitting a function to this data. The fitted function was a sum of three sigmoid functions. This function was chosen because the universal pH indicator consists of three components, each corresponding to a distinct colour transition zone.

2.5. Agarose gel experiments

For the experiments with agarose gel, mini Petri dishes with a diameter of 34 mm were used, each of which was fitted with a 4.5 mm thick 3D-printed insert with a 15.3 mm long and 3 mm wide channel. This geometry was chosen because it can be accurately simulated with a one-dimensional model in our numerical simulations. The design of the insert is depicted in Fig. 2a. To simulate the comparable rate of diffusion and electrophoresis (i.e., the migration of charged species due to the electric field) to that of biological tissue, an agarose gel with the agarose concentration of 0.6 % was used [64]. The experiments were performed with three different media to assess their effects on pH changes: unbuffered medium, bicarbonate buffer, and HEPES buffer. The concentrations for the unbuffered medium (i.e., the NaCl solution) and the bicarbonate buffer solution were chosen to match the concentrations in our simulations (see Table 1). The concentration for the HEPES buffer was chosen to have the same molarity as the bicarbonate buffer, resulting in a concentration of 0.6434 % HEPES, with NaCl added to match the conductivity of the bicarbonate buffer. The corresponding concentrations for all three media were mixed in distilled water. The CO_2 was added to the bicarbonate buffer solution by infusing the distilled water with CO_2 using cartridges of pressurised CO_2 delivered using a pressure regulator, releasing gas into the water during the time required for the water to reach a desired pH level. To prepare the agarose phantoms, 0.6 % agarose powder was dissolved in each of the prepared solutions, heated in the microwave until completely dissolved, and then mixed with 10 % of the volume of the universal pH indicator solution. The resulting liquid agarose solutions were pipetted into the channels of the 3D-printed inserts in the Petri dishes and allowed to cool and solidify into a gel. In the experiments, a pulse waveform consisting of 8 rectangular pulses with a duration of 10 ms each and a repetition rate of 1 s^{-1} was delivered to the agarose gel phantoms. The amplitude of the pulses was either 200 V or 400 V (same as in the model, described in subsection 2.3). This pulse protocol was selected because of its suitability as a protocol for gene electrotransfer. Shorter pulse durations, e.g. in the microsecond range, would limit the observable pH changes, while the use of a larger number of shorter pulses (e.g. 800 pulses of 100 μs each, providing an equivalent on-time to eight 10 ms pulses) would make numerical calculations very challenging. The electrodes were made of 90–10 platinum-iridium alloy, with a diameter of 1 mm and an edge-to-edge distance of 14.3 mm. Three replicates were performed for

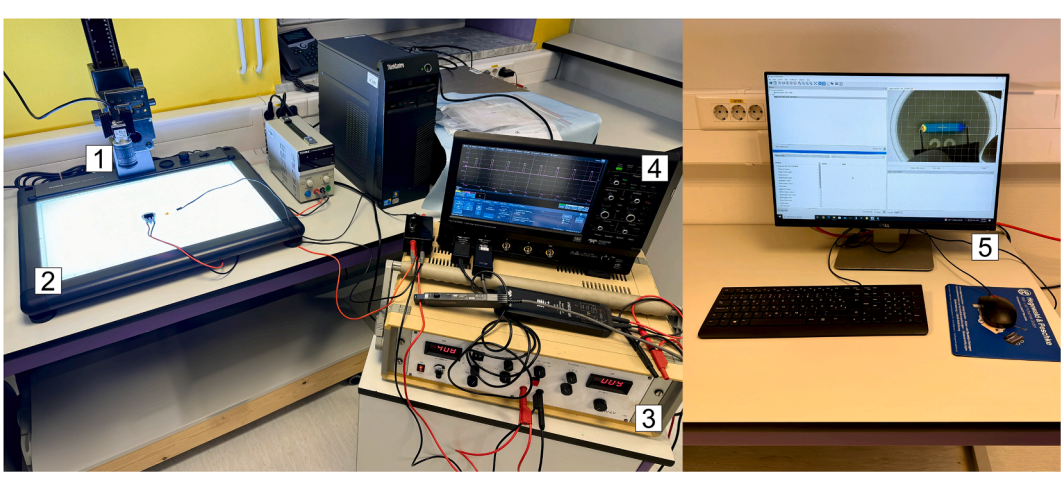

Fig. 1. Experimental setup for agarose gel experiments composed of a camera with a macro lens (1) mounted on a camera stand with an illuminated base (2), a laboratory prototype pulse generator (3), an oscilloscope with voltage and current probes (4), and a PC for recording the experiments (5).

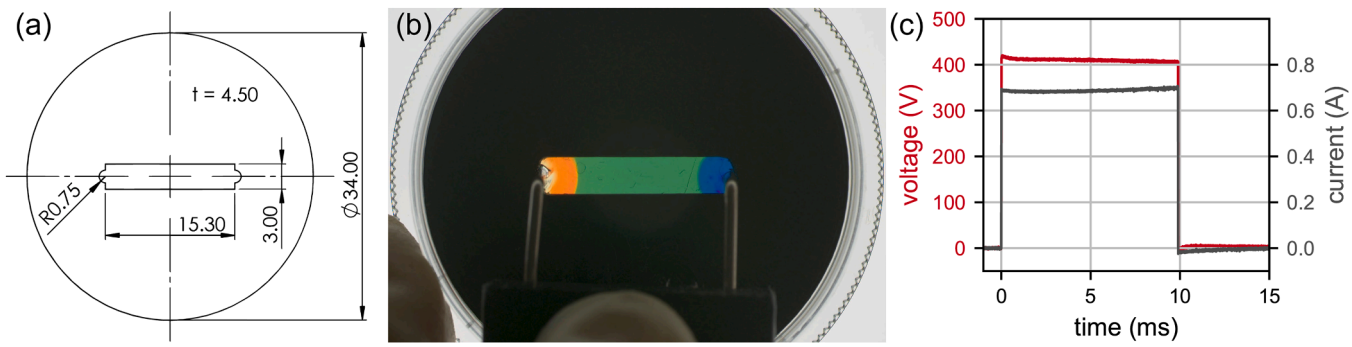

Fig. 2. (a) Design of the 4.5 mm thick 3D-printed insert with a 15.3 mm long and 3 mm wide channel used for agarose gel experiments. Note that all dimensions are in mm. (b) A representative agarose gel experiment performed in a mini Petri dish with the 3D-printed insert. (c) A recorded pulse from an agarose gel experiment.

each experimental condition and the experiments were recorded using the camera system. A representative agarose gel experiment performed in a mini Petri dish with the 3D-printed insert is shown in Fig. 2b, and a recorded pulse (voltage and current) from one of the experiments is shown in Fig. 2c. The post-processing of the experimental data was performed using Python.

3. Results and discussion

3.1. Camera system calibration

Fig. 3 shows the fitted function composed of three sigmoid functions (constituents of Eq. (14)) that relates the colour hue to the pH value and illustrates how the colour hue values vary across different pH levels. The hue values of the captured colours range from about 20 for pH values below 4 to about 260 for pH values above 10. The function demonstrates a useful range from pH 4 to pH 10, within which the hue values are sufficiently distinct for reliable differentiation. This function is crucial for the interpretation of agarose gel experiments, as it allows accurate colour-based pH values determination within the specified range. Outside the pH range of 4 to 10, the colour values are too similar and, therefore, cannot be reliably distinguished. The calibration curve shown in Fig. 3 is defined by the following equation

$$\mathrm{hue}(pH) = 20.20 + \frac{36.25}{1+\exp(-pH\cdot 2.94 + 13.63)} + \frac{135.84}{1+\exp(-pH\cdot 3.17 + 22.22)} + \frac{62.32}{1+\exp(-pH\cdot 3.29 + 30.72)} \quad (14)$$

Eq. (14) consists of a constant offset and three additive sigmoidal constituents of the form $c_1/(1 + \exp/(c_2 \cdot pH + c_3))$. Each of these three terms corresponds to a colour transition of the respective constituent pH indicator forming the universal pH indicator solution. Finding an inverse of the function in Eq. (14) would lead to a poorly defined function at the boundaries, so we solve numerically for pH given a particular hue, thus enabling temporal and spatial determination of the pH value in an agarose gel, i.e., for every pixel of the acquired image at a specific time during observation. Thus, the system allows for accurate (limited by the resolution of the imaging system and motion artifacts) mapping of pH changes in the agarose phantoms and tracking of the pH changes in time during an experiment.

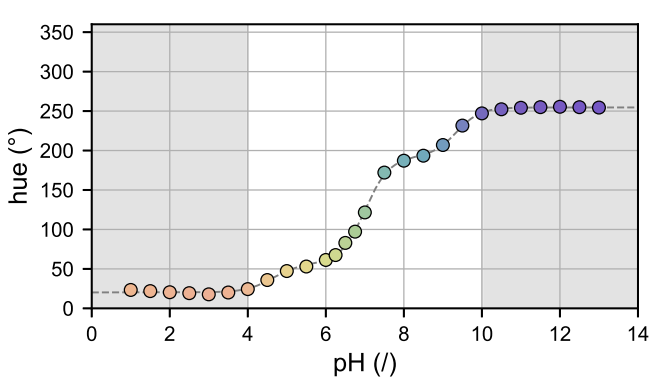

Fig. 3. The calibration curve of the hue value (in degrees) as a function of pH. Note that the usable range for this function is from pH 4 to pH 10, as the hue values outside this range are too similar and, therefore, cannot be reliably distinguished.

The calibration curve should be obtained for each individual laboratory setup and setting to ensure accurate pH reconstruction. Variations in the experimental environment, such as differences in camera type, model, and settings, as well as lighting conditions, can significantly affect the recorded colour hue and consequently the derived pH values. In addition, temperature variations can affect the diffusion coefficients and conductivity, which can affect the formation and diffusion of pH fronts. It is therefore advisable to maintain a stable temperature during the experiments to minimise the variability in obtained results.

3.2. Computational modelling results

The extent to which the pH fronts travelled from the electrodes over time was examined to compare the results of the unbuffered and buffered models. These results are shown in Fig. 4a–c for the unbuffered model and in Fig. 4d–f for the buffered model. Different criteria to define pH fronts were established: Fig. 4a and d portray the entire region of altered pH and track the pH changes around the baseline pH (7.0 in the unbuffered model and 7.4 in the buffered model) within a pH value tolerance of ± 0.05. In Fig. 4b and e, the fronts are tracked for pH values deviating by ± 1.5 from the baseline value. Fig. 4c and f illustrate the range where tissue damage could potentially occur due to extreme pH values (pH below 4.0 at the anode and above 10.6 at the cathode) [60, 65]. The last time point (i.e., at 60 s) corresponds to the experimental results shown in Figs. 5 and 6. The pH fronts in the unbuffered model were approximately twice as large (depending on the definition of the observed pH fronts) as those in the buffered model. In the unbuffered model, the pH fronts are larger at the anode than at the cathode, whereas the opposite is true in the buffered model. This discrepancy could be explained by the fact that the bicarbonate buffer, as prepared and used in our experiments (as opposed to in a living organism), is better at neutralising acidic pH changes, resulting in smaller pH fronts at the anode than at the cathode in the buffered model. The change in the slope of the curve (marked with an arrow) observed at 7.01 s coincides with the delivery of the final pulse in the sequence of eight pulses. During the pulse delivery, pH-altering species are produced and electrophoretically driven away from the electrodes. After the delivery of the last pulse, this electric field-driven migration and production cease. From here on the species diffuse freely at a slower rate compared to the electrophoretic

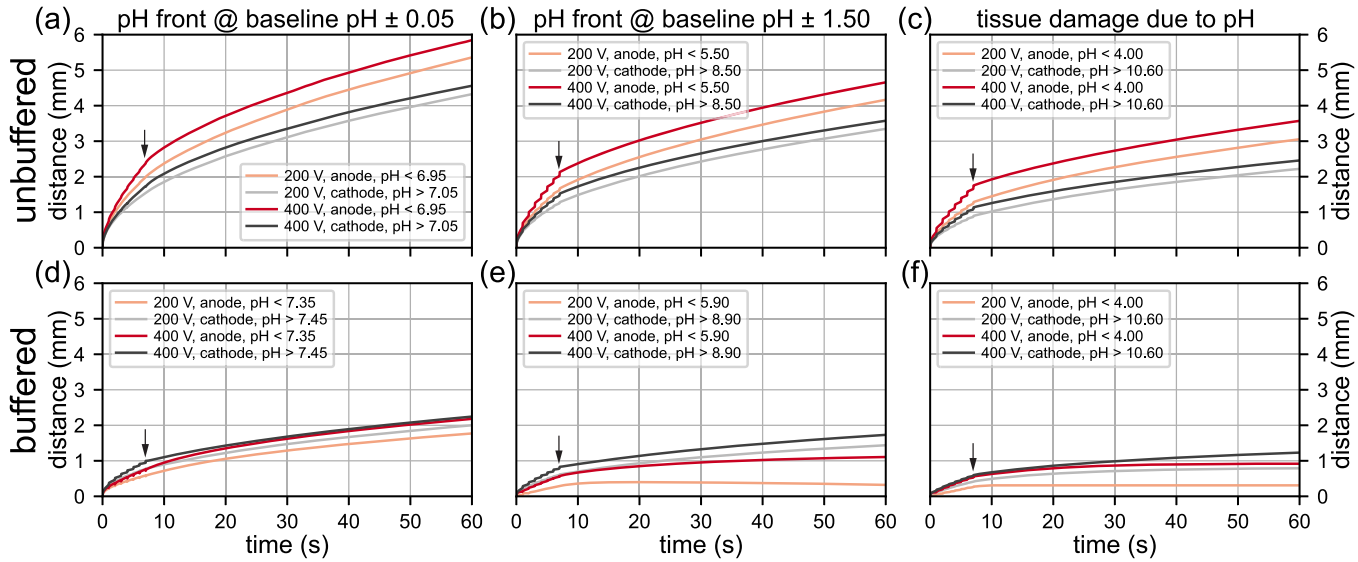

Fig. 4. The time course of the migration of the pH fronts from the anodes and cathodes in both the unbuffered (a-c) and the buffered model (d-e) for two amplitudes of the rectangular pulse waveform, 200 V and 400 V, with different criteria for defining the pH fronts. Note that the baseline pH is different in the unbuffered and the buffered model due to different initial ion concentrations; it is 7.0 in the unbuffered and 7.4 in the buffered model. Arrows indicate the ends of the pulse deliveries at 7.01 s.

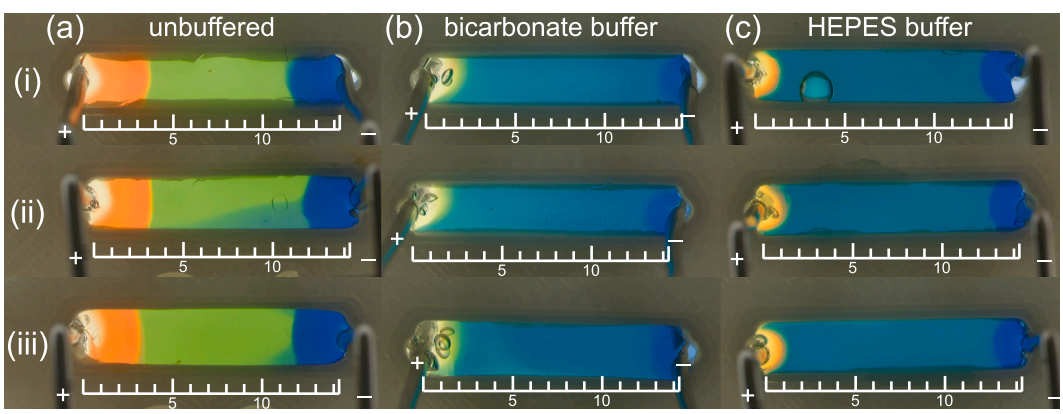

Fig. 5. Three replicates (i, ii, iii) of agarose gel experiments for 8 rectangular pulses with a duration of 10 ms, amplitude of 400 V, and a pulse repetition rate of 1 s^{-1}, performed in (a) the unbuffered medium, (b) the bicarbonate buffer medium, and (c) in the HEPES buffer medium. In order to also investigate the effect of diffusion, a time of 60 seconds from the delivery of the first pulse was selected for the analysis. Note that the scale bar dimensions are expressed in mm.

drag that occurred during the pulses. This transition explains the noticeable change in the slope in the pH front profiles.

3.3. Experimental observations

For each experimental condition (3 different media and 2 different pulse amplitudes), 3 repetitions of the agarose gel experiments were performed. To also capture the effect of diffusion of ionic species after pulse delivery in our investigation, the agarose gel phantoms were analysed 60 s after the start of the pulse delivery (the time point corresponding to the end time point in the graphs shown in Fig. 4). Snapshots extracted from the recorded videos at this time point are shown for the pulse amplitude of 400 V in Fig. 5a for the unbuffered medium, in Fig. 5b for the bicarbonate buffer medium, and in Fig. 5c for the HEPES buffer medium – 3 replicates for each medium. The experimental observations indicated a low variance (high reproducibility) between replicates (i, ii, iii). As expected, a significantly more extensive area of altered pH is observed in the unbuffered medium. However, while the buffer capabilities of the two buffers were comparable (due to being prepared to match in molarity), slight detectable differences between the two buffers were nevertheless observed (Fig. 5b and c). The acidic pH front has a much less extreme pH value in the bicarbonate buffer, even though the front is slightly larger than in the HEPES buffer. Additionally, the delineation between the altered and the baseline pH is much sharper in the HEPES buffer than in the bicarbonate buffer.

The high amplitude of the pulses, both in voltage (and current), is critical, since the rate of hydrolysis and, thus, the amount of produced pH-altering species, is directly proportional to the faradaic charge transfer between the electrode(s) and the electrolytic solution. This transferred charge is, quantitatively, the temporal integral of the ohmic current flowing through the electrolyte solution (i.e., the generator current minus the capacitive current charging and discharging the double-layer capacitance). Due to these high currents flowing through the electrolytic solution (cell suspension, tissue) in electroporation, the resulting pH changes can be substantial, and their quantification is important.

The experimentally determined pH fronts for 8 rectangular pulses with a duration of 10 ms each, delivered at a repetition rate of 1 s^{-1} are shown in Fig. 6 for three different media: the unbuffered medium, the bicarbonate-buffered medium, and the HEPES-buffered medium

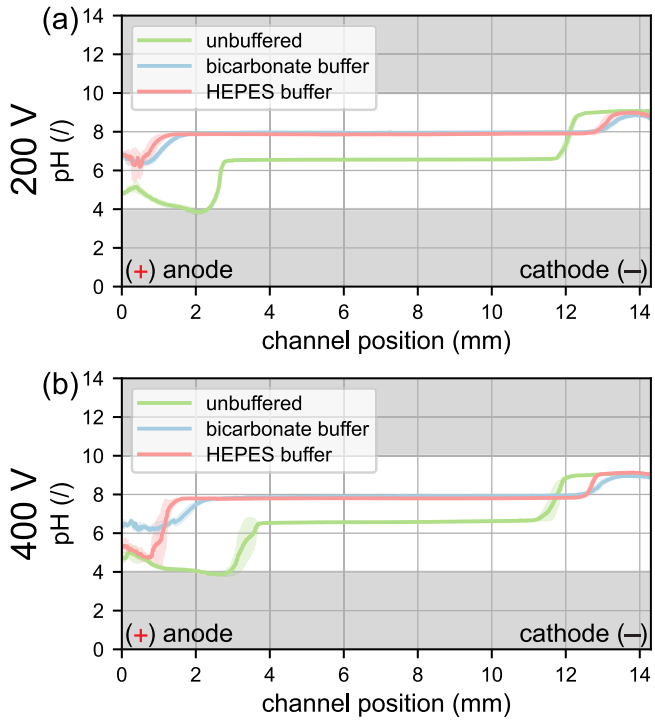

Fig. 6. Experimentally determined pH distributions for 8 rectangular pulses with a duration of 10 ms and a pulse repetition rate of 1 s^{-1} for experiments conducted in unbuffered medium, in bicarbonate-buffered medium, and HEPES-buffered medium. The amplitude of the pulses was 200 V in (a), and 400 V in (b). The shaded areas represent the standard deviations of the averaged values. The results are shown for a time of 60 s to also capture the effect of diffusion in the analysis. The anode is located on the left side (at 0 mm), and the cathode on the right side (at 14.3 mm).

determined 60 s after the start of the pulse delivery. The pulse amplitudes were set to 200 V in Fig. 6a and 400 V in b. In these experiments, the anode was positioned at 0 mm (left side) and the cathode at 14.3 mm (right side). The pH distributions were calculated by averaging the values over the three replicates of the central 50 pixels of the channel width across its entire length, covering the area between the electrodes. The standard deviations of the averaged values are represented by the lightly shaded areas surrounding the averaged values (curves) in Fig. 6. Notably, the pH fronts in the unbuffered medium are approximately twice as large as those observed in the buffered media. There is also a clear difference in baseline pH values between the unbuffered and buffered media, as the baseline pH value of the unbuffered media is around 7.0, and that of the buffered media around is 7.4. As expected, the pH fronts are significantly larger at higher pulse amplitudes. At 200 V pulses, the pH fronts in the bicarbonate and HEPES buffers are quite similar. At 400 V pulses, however, the pH values in the HEPES buffer are more extreme, although the affected regions are smaller compared to those in the bicarbonate buffer. This difference is particularly evident near the anode.

3.4. Comparison of modelling and experimental results

The comparison of the calculated and experimentally determined pH fronts for 8 rectangular pulses each of a duration of 10 ms and a pulse repetition rate of 1 s^{-1} is shown in Fig. 7, determined as before at the 60-second time-point. The experimentally determined pH distributions were calculated by averaging the values of the central 50 pixels of the channel width across its entire length, covering the area between the electrodes, from each of the three replicates performed under identical conditions. The anode was positioned at 0 mm (left side) and the cathode at 14.3 mm (right side). Fig. 7a and b show the results for pulses with the amplitude of 200 V, while Fig. 7c and d show the results for 400 V pulses. The results for the unbuffered medium are shown in Fig. 7a and c, while the results for the bicarbonate-buffered medium are shown in Fig. 7b and d. At the anode side of the unbuffered medium, good agreement between the experimental and simulation results is observed from about 2 mm for an amplitude of 200 V and from about 3 mm for an amplitude of 400 V. However, closer examination reveals an unexpected increase in pH values near the anode in the experimental data, which is unrealistic. This discrepancy is likely due to pH values falling in the undetectable range of our calibration function (shaded in grey in Fig. 3). Also, Fig. 5a shows a lack of colouration near the anode, suggesting that the pH indicator fails to function accurately at these extreme pH values. At the cathode, the experimental pH values are lower than those predicted by the simulations. For the buffered medium, the agreement between simulation and experiment is generally good, with particularly accurate predictions on the anode side.

The simulations predict larger areas of altered pH compared to the experiments, possibly due to an overestimation of the diffusion coefficients (for diffusion in water) in the model (Table 1). Because the model overestimates pH front propagation, the diffusion coefficient values for all species were reduced to 50 % of those listed in Table 1. The simulation results with lower values of the diffusion coefficients are shown in Fig. 7 with dashed lines. These simulation results show improved agreement with the experimental results, particularly for the unbuffered medium at a pulse amplitude of 400 V, but also at 200 V. In the buffered medium, the revised model demonstrates better agreement on the cathode side, albeit slightly less accurate than the model with higher diffusion coefficient on the anode side. Overall, the results indicate that the use of lower diffusion coefficients in the model leads to better agreement with the experimental data, suggesting that the original coefficients (for diffusion in water) may have been overestimated in our case. In our numerical simulations we used a highly refined mesh that effectively reduces the effect of numerical viscosity – a phenomenon where unwanted diffusion effects occur due to the discretisation inherent in numerical simulations. This highly refined mesh ensures that any potential effects of numerical viscosity are negligible and enables accurate representation of the physical processes involved. Further work in varying various species' diffusion coefficients may lead to a better description/prediction of the model with respect to the experiments. It also needs to be considered that tissue diffusion coefficients may differ from those in the agarose gel, potentially limiting the accuracy of the model.

During model development and experimentation with numerical simulations under different pulse parameters and conditions, we have been able to replicate the complex pH front behaviour dependent on pulse protocol parameters (pulse duration and pulse repetition rate). Namely, that the front advances during pulse application and retracts somewhat in the pause between the pulses in the case of the buffered medium. These simulation results corroborate experimental observations obtained in tissue in vivo, such as reported in [27]. However, since pH front retraction can only be observed in the model for pulses delivered at voltages much lower than those we employed in our study, and only for the case of the buffered medium, we opted to keep the discussion and validation of the model as general as possible, and we relegate the analysis at border conditions and the comparison and study of applicability of the model to in vivo work to future work.

4. Conclusions

The aim of the study was to develop a comprehensive mechanistic computational model of the pH changes in tissue during and after pulse application in electroporation applications by means of combined numerical modelling and experimentation. Numerically obtained results were combined with experiments to (1) quantitatively corroborate and validate the model premises by direct comparison of simulation results to a geometrically equivalent/accurate representation of simulated

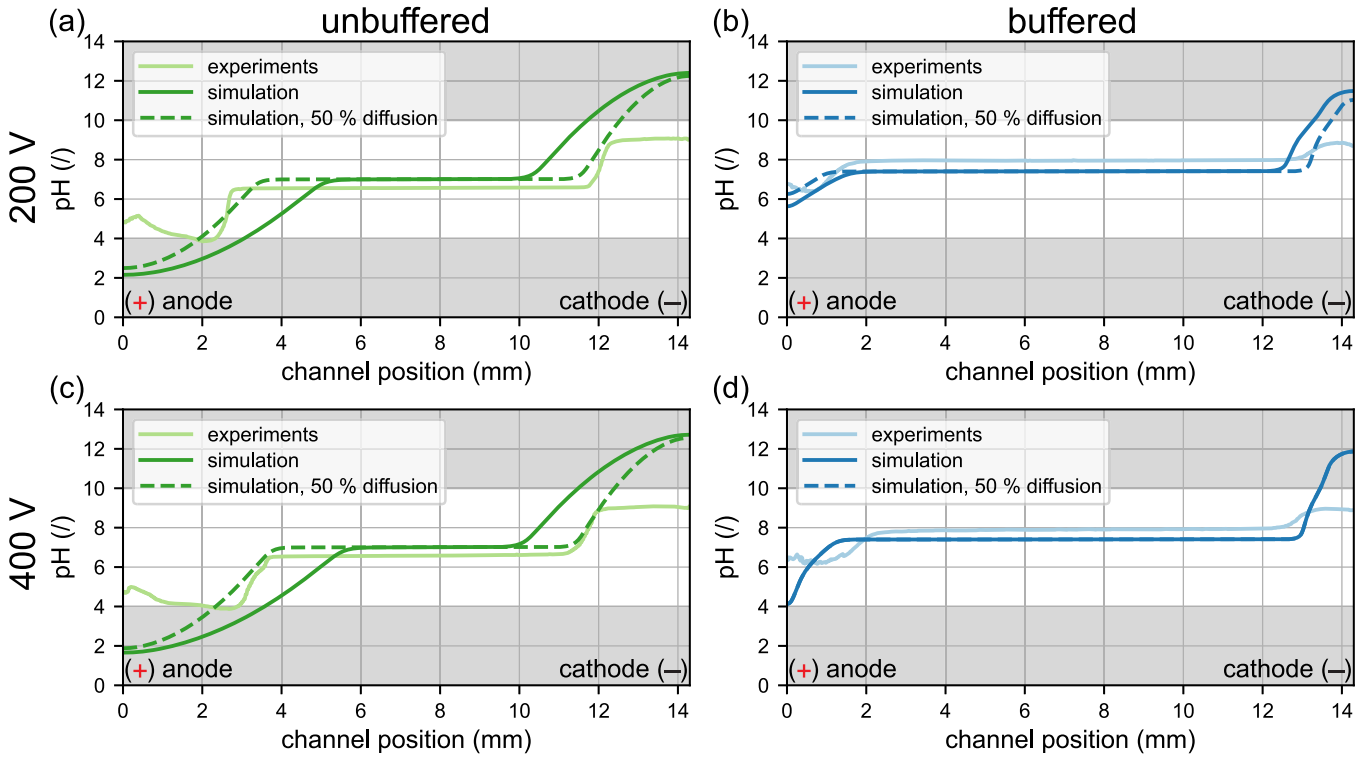

Fig. 7. Comparison of the calculated and experimentally determined pH distributions for 8 rectangular pulses with a duration of 10 ms and a pulse repetition rate of 1 s^{-1}. The amplitude of the pulses was 200 V in (a) and (b), and 400 V in (c) and (d). The results for the unbuffered medium are shown in (a) and (c), while the results for the buffered medium are shown in (b) and (d). The results are shown for a time of 60 s to also include the effect of diffusion in the analysis. The dashed lines represent the results of the models where the diffusion coefficients were reduced to 50 % of the values given in Table 1. The anode is located on the left (at 0 mm), and the cathode on the right (at 14.3 mm).

conditions in vitro, and to (2) obtain insight through experimentation into how accurate and comprehensive the model is in terms of the electrochemical phenomena it manages to capture.

The model is powerful enough to capture the effects of individual pulses and the dynamics of pH front evolution (migration, advancement, retraction) during the pause between the pulses. This is possible due to its construction as a dynamic time-domain model, which accounts for passive diffusion, active field-driven migration of species, and their production and annihilation according to the chemical reaction rates. This high degree of spatio-temporal resolution of the model comes not only with advantages such as deeper insight and understanding of the interplay of the various contributing factors and mechanisms affecting pH front formation and migration, but also with the disadvantage of high numerical complexity and instability, which renders the model difficult for practical use. Future work will focus on improving the robustness of the model in the sense of computational stability.

The results of our work show that the model generates a relatively accurate prediction of the pH front changes within an unbuffered and a buffered media but falls short in terms of absolute accuracy. This can be attributed to inaccurate values of some of the parameters obtained from literature i.e., from already established models in the field. The discrepancy and the need for optimisation in searching for correct ("best-fit") parameter values, as demonstrated by reducing diffusion coefficients (see Fig. 7), warrants further examination and experimentation to determine the origin of the discrepancy – it lies either in the source of the parameters that were adopted for the model, or in a crucial omission from the model in its construction. Either way, experimental observations clearly show there is a need to develop even more complex versions of this electrochemical model, e.g., one that would be capable of accounting for not only diffusion and electrokinetic mechanisms of mass transfer of pH-altering species during pulse application but possibly also for the effect of other mechanisms such as electroosmosis and the interaction between the medium and the pH indicator, both of which have not been examined in our study.

CRediT authorship contribution statement

Rok Šmerc: Writing – review & editing, Writing – original draft, Visualization, Validation, Software, Methodology, Investigation, Formal analysis. **Damijan Miklavčič:** Writing – review & editing, Supervision, Project administration, Funding acquisition, Conceptualization. **Samo Mahnič-Kalamiza:** Writing – review & editing, Writing – original draft, Supervision, Methodology, Investigation, Conceptualization.

Declaration of competing interest

Damijan Miklavčič is the inventor of several patents pending and granted, is receiving royalties, and is consulting for several companies and organizations, which are active in electroporation and electroporation-based technologies and therapies. Other authors report no conflict of interest.

Acknowledgements

The authors acknowledge the support of the Slovenian Research and Innovation Agency (ARIS) under grant P2–0249 Electroporation-based technologies and treatments. This study was conducted within the Infrastructure Programme: Network of research infrastructure centres at the University of Ljubljana (MRIC UL IP-0510), also funded by the Slovenian Research and Innovation Agency (ARIS).

Appendix A. Equations for ionic species production, boundary, and initial conditions

The production of Na^+ and Cl^- ions is zero in both the unbuffered and buffered models

$$R_{Na^+} = R_{Cl^-} = 0. \tag{A.1}$$

In the unbuffered model, the H^+ and OH^- ions can be produced and consumed through the water autoprotolysis reaction

$$R_{H^+} = R_{OH^-} = k_{\mathrm{w,b}}\, c_{H_2O} - k_{\mathrm{w,f}}\, c_{H^+}\, c_{OH^-}, \tag{A.2}$$

where $k_{\mathrm{w,b}}$ and $k_{\mathrm{w,f}}$ are the rate constants of water autoprotolysis reactions in the backward and forward directions, respectively. In the buffered model, the production and consumption of the species H^+, OH^-, HCO_3^-, CO_3^{2-}, and CO_2 are determined according to the water autoprotolysis reaction and the buffer reactions

$$R_{H^+} = k_{\mathrm{w,b}}\cdot c_{H_2O} + k_{\mathrm{b1,b}}\cdot c_{CO_2}\cdot c_{H_2O} - k_{\mathrm{w,f}}\cdot c_{H^+}\cdot c_{OH^-} - k_{\mathrm{b1,f}}\cdot c_{H^+}\cdot c_{HCO_3^-}, \tag{A.3}$$

$$R_{OH^-} = -k_{b2,\mathrm{f}}\cdot c_{CO_2}\cdot c_{OH^-} + k_{\mathrm{b2,b}}\cdot c_{HCO_3^-} - k_{\mathrm{b3,f}}\cdot c_{HCO_3^-}\cdot c_{OH^-} + k_{\mathrm{b3,b}}\cdot c_{CO_3^{2-}} + k_{\mathrm{w,b}}\cdot c_{H_2O} - k_{\mathrm{w,f}}\cdot c_{H^+}\cdot c_{OH^-}, \tag{A.4}$$

$$R_{HCO_3^-} = k_{\mathrm{b1,b}}\cdot c_{CO_2}\cdot c_{H_2O} - k_{\mathrm{b1,f}}\cdot c_{H^+}\cdot c_{HCO_3^-} + k_{\mathrm{b2,f}}\cdot c_{CO_2}\cdot c_{OH^-} - k_{\mathrm{b2,b}} c_{HCO_3^-} - k_{\mathrm{b3,f}}\cdot c_{HCO_3^-}\cdot c_{OH^-} + k_{\mathrm{b3,b}}\cdot c_{CO_3^{2-}}, \tag{A.5}$$

$$R_{CO_2} = -k_{\mathrm{b2,f}}\cdot c_{CO_2}\cdot c_{OH^-} + k_{\mathrm{b2,b}}\cdot c_{HCO_3^-} + k_{\mathrm{b1,f}}\cdot c_{H^+}\cdot c_{HCO_3^-} - k_{\mathrm{b1,b}}\cdot c_{CO_2}\cdot c_{H_2O}, \tag{A.6}$$

$$R_{CO_3^{2-}} = k_{\mathrm{b3,f}}\cdot c_{HCO_3^-}\cdot c_{OH^-} - k_{\mathrm{b3,b}}\cdot c_{CO_3^{2-}}. \tag{A.7}$$

At the electrode surface, the molar flux of the ionic species involved in the electrode reactions is linked to the charge transport of the electrochemical reactions [32,33]. The boundary conditions at the anode surface are therefore

$$\boldsymbol{N}_{H^+}\cdot\boldsymbol{n} = -\frac{j_I}{F}, \tag{A.8}$$

$$\boldsymbol{N}_{Cl^-}\cdot\boldsymbol{n} = \frac{j_{II}}{F}, \tag{A.9}$$

where $\boldsymbol{n}$ is the unit normal vector, F is the Faraday constant, j_I is the current density contribution due to oxygen evolution reaction, and j_{II} is the current density contribution due to chlorine evolution reaction, given by Butler-Volmer equations

$$j_I = j_I^0\left(\exp\left(-\frac{F(\phi + E_I^{\mathrm{eq}})}{2\,R\,T}\right) - \frac{c_{H^+}}{c_{H^+}^0}\cdot\exp\left(\frac{F(\phi + E_I^{\mathrm{eq}})}{2\,R\,T}\right)\right), \tag{A10}$$

$$j_{II} = j_{II}^0\left(\frac{c_{Cl^-}}{c_{Cl^-}^0}\cdot\exp\left(-\frac{F(\phi + E_{II}^{\mathrm{eq}})}{2\,R\,T}\right) - \exp\left(\frac{F(\phi + E_{II}^{\mathrm{eq}})}{2\,R\,T}\right)\right), \tag{A.11}$$

where j_i^0 is the exchange current density of the reaction i, and $\mathrm{E}_i^{\mathrm{eq}}$ is the standard electrode potential of the reaction i. For all the other ionic species, the molar flux at the anode surface is equal to zero, thus

$$\boldsymbol{N}_{OH^-}\cdot\boldsymbol{n} = \boldsymbol{N}_{Na^+}\cdot\boldsymbol{n} = 0 \tag{A.12}$$

in the unbuffered model, and

$$\boldsymbol{N}_{OH^-}\cdot\boldsymbol{n} = \boldsymbol{N}_{Na^+}\cdot\boldsymbol{n} = \boldsymbol{N}_{HCO_3^-}\cdot\boldsymbol{n} = \boldsymbol{N}_{CO_2}\cdot\boldsymbol{n} = \boldsymbol{N}_{CO_3^{2-}}\cdot\boldsymbol{n} = 0 \tag{A13}$$

in the buffered model. At the cathode surface, the boundary condition is

$$\boldsymbol{N}_{OH^-}\cdot\boldsymbol{n} = \frac{j_{III}}{F}, \tag{A.14}$$

where j_{III} is the current density contribution due to hydrogen evolution reaction

$$j_{III} = j_{III}^0\left(\left(\frac{c_{OH^-}}{c_{OH^-}^0}\right)^2\cdot\exp\left(-\frac{3F(\phi + E_{III}^{\mathrm{eq}})}{2\,R\,T}\right) - \exp\left(\frac{F(\phi + E_{III}^{\mathrm{eq}})}{2\,R\,T}\right)\right) \tag{A.15}$$

For all the other ionic species, the molar flux at the cathode surface is equal to zero, thus

$$\boldsymbol{N}_{H^+}\cdot\boldsymbol{n} = \boldsymbol{N}_{Na^+}\cdot\boldsymbol{n} = \boldsymbol{N}_{Cl^-}\cdot\boldsymbol{n} = 0 \tag{A.16}$$

in the unbuffered model, and

$$\boldsymbol{N}_{H^+}\cdot\boldsymbol{n} = \boldsymbol{N}_{Na^+}\cdot\boldsymbol{n} = \boldsymbol{N}_{Cl^-}\cdot\boldsymbol{n} = \boldsymbol{N}_{HCO_3^-}\cdot\boldsymbol{n} = \boldsymbol{N}_{CO_2}\cdot\boldsymbol{n} = \boldsymbol{N}_{CO_3^{2-}}\cdot\boldsymbol{n} = 0 \tag{A.17}$$

in the buffered model. Since there are initially no concentration gradients in the electrolyte, the initial conditions are

$$\nabla c_i = 0 \text{ at } t = 0, \tag{A.18}$$

$$c_i = c_i^0. \tag{A.19}$$

Data availability

Data will be made available on request.

References

[1] E. Neumann, K. Rosenheck, Permeability changes induced by electric impulses in vesicular membranes, J. Membrain Biol. 10 (1972) 279–290, https://doi.org/10.1007/BF01867861.

[2] T. Kotnik, G. Pucihar, D. Miklavčič, The cell in the electric field, in: S.T. Kee, J. Gehl, E.W. Lee (Eds.), Clinical Aspects of Electroporation, Springer New York, New York, NY, 2011, pp. 19–29, https://doi.org/10.1007/978-1-4419-8363-3_3.

[3] T. Kotnik, L. Rems, M. Tarek, D. Miklavčič, Membrane electroporation and electropermeabilization: mechanisms and models, Annu. Rev. Biophys. 48 (2019) 63–91, https://doi.org/10.1146/annurev-biophys-052118-115451.

[4] S. Haberl, D. Miklavcic, G. Sersa, W. Frey, B. Rubinsky, Cell membrane electroporation-Part 2: the applications, IEEE Electr. Insul. Mag. 29 (2013) 29–37, https://doi.org/10.1109/MEI.2013.6410537.

[5] M.L. Yarmush, A. Golberg, G. Serša, T. Kotnik, D. Miklavčič, Electroporation-based technologies for medicine: principles, applications, and challenges, Annu. Rev. Biomed. Eng. 16 (2014) 295–320, https://doi.org/10.1146/annurev-bioeng-071813-104622.

[6] T. Kotnik, W. Frey, M. Sack, S. Haberl Meglič, M. Peterka, D. Miklavčič, Electroporation-based applications in biotechnology, Trend. Biotechnol. 33 (2015) 480–488, https://doi.org/10.1016/j.tibtech.2015.06.002.

[7] S. Mahnič-Kalamiza, E. Vorobiev, D. Miklavčič, Electroporation in food processing and biorefinery, J. Membran. Biol. 247 (2014) 1279–1304, https://doi.org/10.1007/s00232-014-9737-x.

[8] G. Saldaña, I. Álvarez, S. Condón, J. Raso, Microbiological aspects related to the feasibility of PEF technology for food pasteurization, Crit. Rev. Food Sci. Nutr. 54 (2014) 1415–1426, https://doi.org/10.1080/10408398.2011.638995.

[9] S. Sachdev, T. Potočnik, L. Rems, D. Miklavčič, Revisiting the role of pulsed electric fields in overcoming the barriers to in vivo gene electrotransfer, Bioelectrochemistry 144 (2022) 107994, https://doi.org/10.1016/j.bioelechem.2021.107994.

[10] B. Geboers, H.J. Scheffer, P.M. Graybill, A.H. Ruarus, S. Nieuwenhuizen, R.S. Puijk, P.M. Van Den Tol, R.V. Davalos, B. Rubinsky, T.D. De Gruijl, D. Miklavčič, M. R. Meijerink, High-voltage electrical pulses in oncology: irreversible electroporation, electrochemotherapy, gene electrotransfer, electrofusion, and electroimmunotherapy, Radiology 295 (2020) 254–272, https://doi.org/10.1148/radiol.2020192190.

[11] R. Heller, L.C. Heller, Gene electrotransfer clinical trials. Advances in Genetics, Elsevier, 2015, pp. 235–262, https://doi.org/10.1016/bs.adgen.2014.10.006.

[12] C. Rosazza, S. Haberl Meglic, A. Zumbusch, M.-P. Rols, D. Miklavcic, Gene Electrotransfer, A mechanistic perspective, CGT 16 (2016) 98–129, https://doi.org/10.2174/1566523216666160331130040.

[13] A. Sugrue, V. Vaidya, C. Witt, C.V. DeSimone, O. Yasin, E. Maor, A.M. Killu, S. Kapa, C.J. McLeod, D. Miklavčič, S.J. Asirvatham, Irreversible electroporation for catheter-based cardiac ablation: a systematic review of the preclinical experience, J. Interv. Card. Electrophysiol. 55 (2019) 251–265, https://doi.org/10.1007/s10840-019-00574-3.

[14] A. Verma, L. Boersma, D.E. Haines, A. Natale, F.E. Marchlinski, P. Sanders, H. Calkins, D.L. Packer, J. Hummel, B. Onal, S. Rosen, K.-H. Kuck, G. Hindricks, B. Wilsmore, First-in-human experience and acute procedural outcomes using a novel pulsed field ablation system: the PULSED AF pilot trial, Circ.: Arrhythm. Electrophysiol. 15 (2022) e010168, https://doi.org/10.1161/CIRCEP.121.010168.

[15] V.Y. Reddy, E.P. Gerstenfeld, A. Natale, W. Whang, F.A. Cuoco, C. Patel, S. E. Mountantonakis, D.N. Gibson, J.D. Harding, C.R. Ellis, K.A. Ellenbogen, D. B. DeLurgio, J. Osorio, A.B. Achyutha, C.W. Schneider, A.S. Mugglin, E. M. Albrecht, K.M. Stein, J.W. Lehmann, M. Mansour, Pulsed field or conventional thermal ablation for paroxysmal atrial fibrillation, N. Engl. J. Med. 389 (2023) 1660–1671, https://doi.org/10.1056/NEJMoa2307291.

[16] A. Verma, D.E. Haines, L.V. Boersma, N. Sood, A. Natale, F.E. Marchlinski, H. Calkins, P. Sanders, D.L. Packer, K.-H. Kuck, G. Hindricks, B. Onal, J. Cerkvenik, H. Tada, D.B. DeLurgio, on behalf of the PULSED AF investigators, pulsed field ablation for the treatment of atrial fibrillation: PULSED AF pivotal trial, Circulation 147 (2023) 1422–1432, https://doi.org/10.1161/CIRCULATIONAHA.123.063988.

[17] K.-R.J. Chun, D. Miklavčič, K. Vlachos, S. Bordignon, D. Scherr, P. Jais, B. Schmidt, State-of-the-art pulsed field ablation for cardiac arrhythmias: ongoing evolution and future perspective, Europace 26 (2024) euae134, https://doi.org/10.1093/europace/euae134.

[18] S. Mahnič-Kalamiza, D. Miklavčič, Scratching the electrode surface: insights into a high-voltage pulsed-field application from in vitro & in silico studies in indifferent fluid, Electrochim. Acta 363 (2020) 137187, https://doi.org/10.1016/j.electacta.2020.137187.

[19] P.A. Garcia, R.V. Davalos, D. Miklavcic, A numerical investigation of the electric and thermal cell kill distributions in electroporation-based therapies in tissue, PLoS ONE 9 (2014) e103083, https://doi.org/10.1371/journal.pone.0103083.

[20] C. Rossmanna, D. Haemmerich, Review of temperature dependence of thermal properties, dielectric properties, and perfusion of biological tissues at hyperthermic and ablation temperatures, Crit. Rev. Biomed. Eng. 42 (2014) 467–492, https://doi.org/10.1615/CritRevBiomedEng.2015012486.

[21] E.M. Dunki-Jacobs, P. Philips, R.C.G. Martin Ii, Evaluation of thermal injury to liver, pancreas and kidney during irreversible electroporation in an in vivo experimental model, Brit. J. Surg. 101 (2014) 1113–1121, https://doi.org/10.1002/bjs.9536.

[22] K.N. Aycock, R.V. Davalos, Irreversible electroporation: background, theory, and review of recent developments in clinical oncology, Bioelectricity 1 (2019) 214–234, https://doi.org/10.1089/bioe.2019.0029.

[23] P. Agnass, E. Van Veldhuisen, M.J.C. Van Gemert, C.W.M. Van Der Geld, K.P. Van Lienden, T.M. Van Gulik, M.R. Meijerink, M.G. Besselink, H.P. Kok, J. Crezee, Mathematical modeling of the thermal effects of irreversible electroporation for in vitro, in vivo, and clinical use: a systematic review, Int. J. Hypertherm. 37 (2020) 486–505, https://doi.org/10.1080/02656736.2020.1753828.

[24] E. Nilsson, J. Berendson, E. Fontes, Impact of chlorine and acidification in the electrochemical treatment of tumours, J. Appl. Electrochem. 30 (2000) 1321–1333, https://doi.org/10.1023/A:1026560806158.

[25] E. Nilsson, E. Fontes, Mathematical modelling of physicochemical reactions and transport processes occurring around a platinum cathode during the electrochemical treatment of tumours, Bioelectrochemistry 53 (2001) 213–224, https://doi.org/10.1016/S0302-4598(01)00097-6.

[26] P. Turjanski, N. Olaiz, F. Maglietti, S. Michinski, C. Suárez, F.V. Molina, G. Marshall, The role of pH fronts in reversible electroporation, PLoS ONE 6 (2011) e17303, https://doi.org/10.1371/journal.pone.0017303.

[27] M. Marino, N. Olaiz, E. Signori, F. Maglietti, C. Suárez, S. Michinski, G. Marshall, pH fronts and tissue natural buffer interaction in gene electrotransfer protocols, Electrochim. Acta 255 (2017) 463–471, https://doi.org/10.1016/j.electacta.2017.09.021.

[28] X. Wang, H.J. Lim, A. Son, Characterization of denaturation and renaturation of DNA for DNA hybridization, Environ. Health. Toxicol. 29 (2014) e2014007, https://doi.org/10.5620/eht.2014.29.e2014007.

[29] T. Potočnik, S. Sachdev, T. Polajžer, A. Maček Lebar, D. Miklavčič, Efficient gene transfection by electroporation—in vitro and in silico study of pulse parameters, Appl. Sci. 12 (2022) 8237, https://doi.org/10.3390/app12168237.

[30] T. Potočnik, A. Maček Lebar, Š. Kos, M. Reberšek, E. Pirc, G. Serša, D. Miklavčič, Effect of experimental electrical and biological parameters on gene transfer by electroporation: a systematic review and meta-analysis, Pharmaceutics 14 (2022) 2700, https://doi.org/10.3390/pharmaceutics14122700.

[31] D. Miklavčič, A. Fajgelj, G. Serša, Tumour treatment by direct electric current: electrode material deposition, Bioelectrochem. Bioenerget. 35 (1994) 93–97, https://doi.org/10.1016/0302-4598(94)87017-9.

[32] E. Nilsson, J. Berendson, E. Fontes, Development of a dosage method for electrochemical treatment of tumours: a simplified mathematical model, Bioelectrochem. Bioenerget. 47 (1998) 11–18, https://doi.org/10.1016/S0302-4598(98)00157-3.

[33] E. Nilsson, J. Berendson, E. Fontes, Electrochemical treatment of tumours: a simplified mathematical model, J. Electroanalyt. Chem. 460 (1999) 88–99, https://doi.org/10.1016/S0022-0728(98)00352-0.

[34] E. Nilsson, H. Von Euler, J. Berendson, A. Thörne, P. Wersäll, I. Näslund, A.-S. Lagerstedt, K. Narfström, J.M. Olsson, Electrochemical treatment of tumours, Bioelectrochemistry 51 (2000) 1–11, https://doi.org/10.1016/S0302-4598(99)00073-2.

[35] H. Von Euler, A. Söderstedt, A. Thörne, J.M. Olsson, G. Yongqing, Cellular toxicity induced by different pH levels on the R3230AC rat mammary tumour cell line. An in vitro model for investigation of the tumour destructive properties of electrochemical treatment of tumours, Bioelectrochemistry 58 (2002) 163–170, https://doi.org/10.1016/S1567-5394(02)00154-8.

[36] H.M.C. Ciria, M.M. González, L.O. Zamora, L.E.B. Cabrales, G.V. Sierra González, L. O. de Oliveira, R. Zanella, A.C. Buzaid, O. Parise, L.M. Brito, C.A.A. Teixeira, M. das N. Gomes, G. Moreno, V. Feo da Veiga, M. Telló, C. Holandino, Antitumor effects of electrochemical treatment, Chin. J. Cancer Res. 25 (2013) 223–234, https://doi.org/10.3978/j.issn.1000-9604.2013.03.03.

[37] M. Phillips, L. Rubinsky, A. Meir, N. Raju, B. Rubinsky, Combining electrolysis and electroporation for tissue ablation, Technol. Cancer Res. Treat. 14 (2015) 395–410, https://doi.org/10.1177/1533034614560102.

[38] M. Phillips, H. Krishnan, N. Raju, B. Rubinsky, Tissue ablation by a synergistic combination of electroporation and electrolysis delivered by a single pulse, Ann. Biomed. Eng. 44 (2016) 3144–3154, https://doi.org/10.1007/s10439-016-1624-4.

[39] L. Rubinsky, E. Guenther, P. Mikus, M. Stehling, B. Rubinsky, Electrolytic effects during tissue ablation by electroporation, Technol. Cancer Res. Treat. 15 (2016) NP95–NP103, https://doi.org/10.1177/1533034615601549.
[40] H.B. Kim, J.H. Chung, Incorporation of reversible electroporation into electrolysis accelerates apoptosis for rat liver tissue, Technol. Cancer Res. Treat. 19 (2020) 153303382094805, https://doi.org/10.1177/1533033820948051.
[41] N.R. Rajagopalan, T. Munawar, M.C. Sheehan, M. Fujimori, W.-R. Vista, T. Wimmer, N.B. Gutta, S.B. Solomon, G. Srimathveeravalli, Electrolysis products, reactive oxygen species and ATP loss contribute to cell death following irreversible electroporation with microsecond-long pulsed electric fields, Bioelectrochemistry 155 (2024) 108579, https://doi.org/10.1016/j.bioelechem.2023.108579.
[42] A. Vižintin, S. Marković, J. Ščančar, D. Miklavčič, Electroporation with nanosecond pulses and bleomycin or cisplatin results in efficient cell kill and low metal release from electrodes, Bioelectrochemistry 140 (2021) 107798, https://doi.org/10.1016/j.bioelechem.2021.107798.
[43] E. Radzevičiūtė-Valčiukė, J. Gečaitė, A. Želvys, A. Zinkevičienė, R. Žalnėravičius, V. Malyško-Ptašinskė, A. Nemeikaitė-Čenienė, V. Kašėta, N. German, J. Novickij, A. Ramanavičienė, J. Kulbacka, V. Novickij, Improving nonviral gene delivery using MHz bursts of nanosecond pulses and gold nanoparticles for electric field amplification, Pharmaceutics 15 (2023) 1178, https://doi.org/10.3390/pharmaceutics15041178.
[44] K. Balantič, P. Kramar, D. Miklavčič, *In Silico* numerical model of aluminum and iron dissolution during electric pulse application for electroporation, Bioelectricity (2024), https://doi.org/10.1089/bioe.2023.0026 bioe.2023.0026.
[45] A. Meir, M. Hjouj, L. Rubinsky, B. Rubinsky, Magnetic resonance imaging of electrolysis, Sci. Rep. 5 (2015) 8095, https://doi.org/10.1038/srep08095.
[46] A. Meir, B. Rubinsky, Electrical impedance tomography of electrolysis, PLoS ONE 10 (2015) e0126332, https://doi.org/10.1371/journal.pone.0126332.
[47] J. Morren, B. Roodenburg, S.W.H. De Haan, Electrochemical reactions and electrode corrosion in pulsed electric field (PEF) treatment chambers, Innov. Food Sci. Emerg. Technolog. 4 (2003) 285–295, https://doi.org/10.1016/S1466-8564(03)00041-9.
[48] N. Meneses, H. Jaeger, D. Knorr, pH-changes during pulsed electric field treatments — numerical simulation and in situ impact on polyphenoloxidase inactivation, Innov. Food Sci. Emerg. Technolog. 12 (2011) 499–504, https://doi.org/10.1016/j.ifset.2011.07.001.
[49] G. Pataro, G.M.J. Barca, G. Donsì, G. Ferrari, On the modelling of the electrochemical phenomena at the electrode-solution interface of a PEF treatment chamber: effect of electrical parameters and chemical composition of model liquid food, J. Food Eng. 165 (2015) 45–51, https://doi.org/10.1016/j.jfoodeng.2015.05.010.
[50] D. Miklavčič, G. Serša, M. Kryžanowski, S. Novakovič, F. Bobanović, R. Golouh, L. Vodovnik, Tumor treatment by direct electric current-tumor temperature and pH, electrode material and configuration, Bioelectrochem. Bioenerget. 30 (1993) 209–220, https://doi.org/10.1016/0302-4598(93)80080-E.
[51] P. Turjanski, N. Olaiz, P. Abou-Adal, C. Suárez, M. Risk, G. Marshall, pH front tracking in the electrochemical treatment (EChT) of tumors: experiments and simulations, Electrochim. Acta 54 (2009) 6199–6206, https://doi.org/10.1016/j.electacta.2009.05.062.
[52] N. Olaiz, C. Suárez, M. Risk, F. Molina, G. Marshall, Tracking protein electrodenaturation fronts in the electrochemical treatment of tumors, Electrochem. Commun. 12 (2010) 94–97, https://doi.org/10.1016/j.elecom.2009.10.044.
[53] N. Olaiz, F. Maglietti, C. Suárez, F.V. Molina, D. Miklavcic, L. Mir, G. Marshall, Electrochemical treatment of tumors using a one-probe two-electrode device, Electrochim. Acta 55 (2010) 6010–6014, https://doi.org/10.1016/j.electacta.2010.05.057.
[54] E. Luján, H. Schinca, N. Olaiz, S. Urquiza, F.V. Molina, P. Turjanski, G. Marshall, Optimal dose-response relationship in electrolytic ablation of tumors with a one-probe-two-electrode device, Electrochim. Acta 186 (2015) 494–503, https://doi.org/10.1016/j.electacta.2015.10.147.
[55] E.M. Calzado, H. Schinca, L.E.B. Cabrales, F.M. García, P. Turjanski, N. Olaiz, Impact of permeabilization and pH effects in the electrochemical treatment of tumors: experiments and simulations, Appl. Math. Model. 74 (2019) 62–72, https://doi.org/10.1016/j.apm.2019.04.041.
[56] A. Mokhtare, M. Shiv Krishna Reddy, V.A. Roodan, E.P. Furlani, A. Abbaspourrad, The role of pH fronts, chlorination and physicochemical reactions in tumor necrosis in the electrochemical treatment of tumors: a numerical study, Electrochim. Acta 307 (2019) 129–147, https://doi.org/10.1016/j.electacta.2019.03.148.
[57] F. Maglietti, S. Michinski, N. Olaiz, M. Castro, C. Suárez, G. Marshall, The role of Ph fronts in tissue electroporation based treatments, PLoS ONE 8 (2013) e80167, https://doi.org/10.1371/journal.pone.0080167.
[58] Z.S. Salameh, K.N. Aycock, N. Alinezhadbalalami, K.M. Imran, I.H. McKillop, I. C. Allen, R.V. Davalos, Harnessing the electrochemical effects of electroporation-based therapies to enhance anti-tumor immune responses, Ann. Biomed. Eng. 52 (2024) 48–56, https://doi.org/10.1007/s10439-023-03403-x.
[59] N. Olaiz, E. Signori, F. Maglietti, A. Soba, C. Suárez, P. Turjanski, S. Michinski, G. Marshall, Tissue damage modeling in gene electrotransfer: the role of pH, Bioelectrochemistry 100 (2014) 105–111, https://doi.org/10.1016/j.bioelechem.2014.05.001.
[60] E. Luján, M. Marino, N. Olaiz, G. Marshall, Towards an optimal dose-response relationship in gene electrotransfer protocols, Electrochim. Acta 319 (2019) 1002–1011, https://doi.org/10.1016/j.electacta.2019.07.029.
[61] T. Jarm, M. Cemazar, D. Miklavcic, G. Sersa, Antivascular effects of electrochemotherapy: implications in treatment of bleeding metastases, Expert. Rev. Anticancer Ther. 10 (2010) 729–746, https://doi.org/10.1586/era.10.43.
[62] J.S. Newman, K.E. Thomas-Alyea, Electrochemical Systems, J. Wiley, Hoboken, N. J, 2004, 3rd ed.
[63] M. Pavlin, K. Flisar, M. Kandušer, The role of electrophoresis in gene electrotransfer, J. Membran. Biol. 236 (2010) 75–79, https://doi.org/10.1007/s00232-010-9276-z.
[64] E. Albor-Ramírez, M. Reyes-Alberto, L.M. Vidal-Flores, E. Gutierrez-Herrera, M. A. Padilla-Castañeda, Agarose gel characterization for the fabrication of brain tissue phantoms for infrared multispectral vision systems, Gels 9 (2023) 944, https://doi.org/10.3390/gels9120944.
[65] N.R. Perkons, E.J. Stein, C. Nwaezeapu, J.C. Wildenberg, K. Saleh, R. Itkin-Ofer, D. Ackerman, M.C. Soulen, S.J. Hunt, G.J. Nadolski, T.P. Gade, Electrolytic ablation enables cancer cell targeting through pH modulation, Commun. Biol. 1 (2018) 48, https://doi.org/10.1038/s42003-018-0047-1.